EVIDENT

16 Advances in Microscale Photonics

Characterization Techniques for Materials in Volume

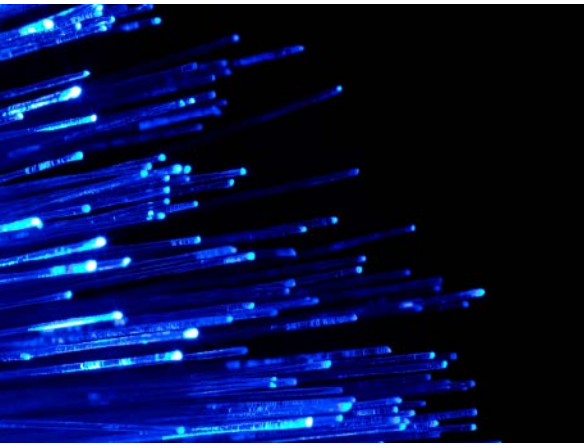

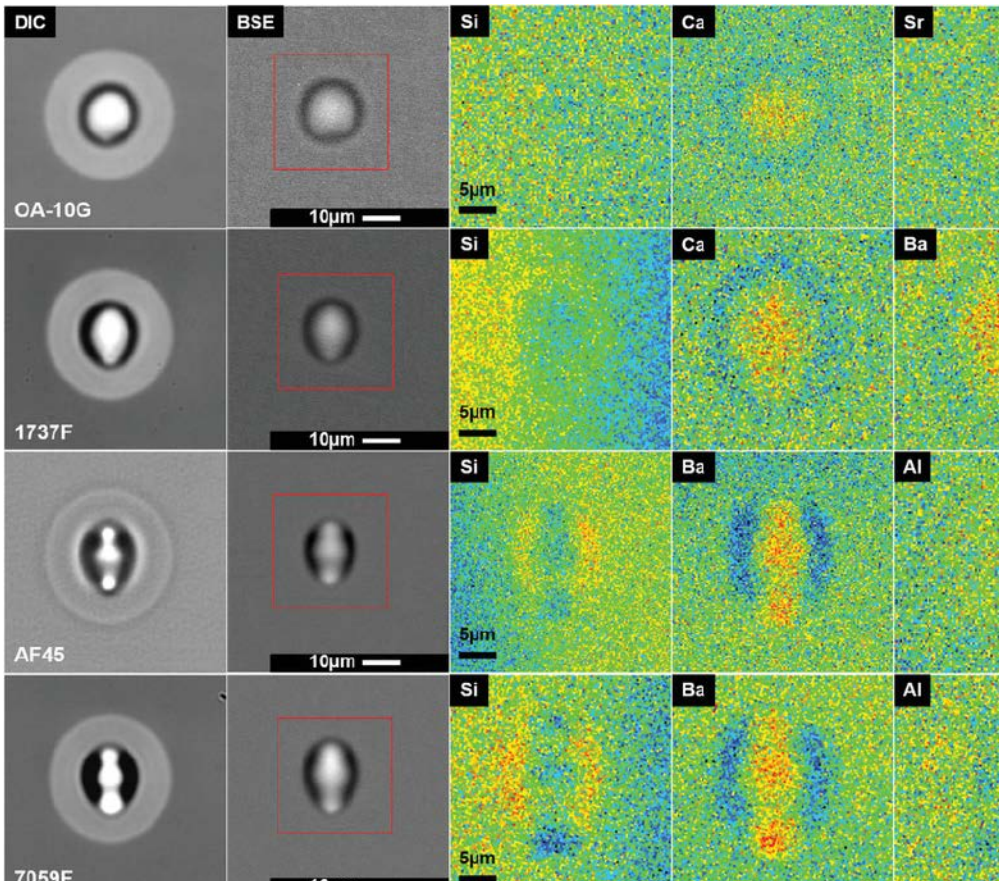

OLYMPUS

WILEY

Contents

Imprint

© Wiley-VCH GmbH
Boschstr. 12,
69469 Weinheim, Germany
Email: info@wiley-vch.de
Editors:
Dr. Cecilia Kruszynski &
Róisín Murtagh

Advances in microscale photonics: Characterization techniques for materials in volume

Photonics is the science that deals with the handling of ultraviolet, visible, and infrared light through linear and non-linear optical effects. Moreover, it involves all the possible technological applications of light manipulation, from energy generation to communications and information engineering.

Microphotonic research is concerned with the study of the properties of light in the mentioned wavelength ranges as well as with the development of tools and technologies to exploit optical phenomena. This includes optical bandgap crystals and colloidal metals, among others.

The term "microphotonic" usually refers to a whole branch of technology dealing with the guiding of light at the microscale, which is of particular interest in optical networks. In particular, it is related to devices and integrated systems that emit, transmit, detect, and process light photons.

In microphotonics, at least two different materials having a high contrast of refractive index *(n)* are required to confine light. Generally speaking, microphotonics is based on Fresnel's reflection for light guiding. If photons remain mainly in the higher *n* material, the light confinement is due to total internal reflection. On the other hand, if confinement is caused by multiple distributed Fresnel reflections, the device in question is called a photonic crystal. Many geometries are used in microphotonics, including optical waveguides, optical microcavities, and arrayed waveguide gratings, for example.

Photonic crystals are dielectric materials that reflect a wavelength range almost perfectly; because of that, they are usually known as perfect mirrors. Other devices in the field include micro mirrors and photonic wire waveguides. These tools are used in shaping the flow of light, a famous saying to describe the ultimate goal of microphotonics and photonics. In general, photonic crystals serve as structures that allow manipulation, confinement, and control of light in one, two, or three dimensions.

This field has numerous applications in areas such as telecommunications, sensing, and biomedical imaging. Biology, for example, is particularly interested in microphotonics, as demonstrated by the development of biophotonic chips designed to increase efficiency in terms of photonic performance or the luminescent signal emitted by fluorescent markers employed in biological chips.

One important aspect of microscale photonics is the characterization of materials in volume. This involves the measurement of various optical properties of materials, such as refractive index, absorption, and scattering, as well as the determination of their physical properties, such as thickness and roughness.

◀ back to content

Recent advances in microscale photonics have led to the development of several techniques for characterizing materials in volume. One such technique is optical coherence tomography (OCT), which uses low-coherence interferometry to create high-resolution, cross-sectional images of materials.

Another technique for characterizing materials in volume is confocal microscopy, which uses a laser beam to illuminate a sample and a pinhole aperture to eliminate out-of-focus light. This technique allows for high-resolution, three-dimensional imaging of biological tissues and other materials. One important application of confocal microscopy in microphotonics is in the characterization of photonic structures, such as photonic crystals, waveguides, and resonators. Confocal microscopy enables high-resolution imaging of the complex three-dimensional geometries often found in these structures, in all three dimensions. This information can be used to optimize the design of these structures for specific applications, such as in telecommunications or sensing.

Optical profilometry is another important tool for characterizing the physical properties of photonic structures and devices. The method is based on the interference of a reference and a sample laser beam that scan the sample to get information about the height variations and roughness of a given surface. This technique is particularly useful for the measurement of the surface roughness of photonic structures, such as waveguides, resonators, and diffractive elements. The surface roughness can affect the performance of these structures, and optical profilometry allows for the precise measurement of surface roughness at the micro- and nanoscale. This information can be used to optimize the fabrication processes for these structures and to improve their performance. This technique is also useful for measuring the thickness and refractive index of thin films and coatings used in photonic devices. These measurements are important for optimizing the performance of devices such as antireflection coatings, thin-film filters, and surface plasmon resonance sensors.

Another example is given by ultrafast coherent spectroscopy, a technique used to study the behavior of molecules and materials on extremely short timescales. It combines the use of ultrafast laser pulses with coherent detection methods to measure the time-dependent response of a sample to various perturbations, such as light or electric fields. It is used to study the properties of photonic materials and devices, such as waveguides and optical fibers. By measuring the response of these materials to ultrafast pulses of light, researchers can gain insight into their optical properties and behavior.

Other advances in microscale photonics include the development of techniques for manipulating light on the nanoscale such as plasmonic and metamaterial techniques as well as the use of micro- and nanofabrication techniques to create photonic devices with unprecedented precision.

The advances in microscale photonics have led to numerous breakthroughs in the field of photonics, and have the potential to enable a wide range of new applications in fields, such as medicine, telecommunications, and sensing, among others.

◀ back to content

01 Electrohydrodynamic inkjet-printed for applications in mid-infrared meta-optics

Adapted from Brunner *et al.* (2022)

A novel printing solution is presented containing a titania alkoxide precursor that is compatible with electrohydrodynamic inkjet (EHDIJ) printing and capable of producing final printed features of 1 μm and below; the highest resolution features ever reported for this family of materials and this method. This solution is used to fabricate the first EHDIJ printed and functioning mid-infrared meta-optics lens, capable of focusing 5 μm light. The features of continuum and dropwise printing modes as well as the quality of the final meta-optical micro-scale lenses were characterized using an Olympus OLS4100 optical profilometer.

INTRODUCTION

The past two decades have seen significant research and development efforts toward additive manufacturing of functional materials using inkjet printing and direct-write 3D printing techniques for applications such as displays and flexible electronics.[1,2] In the case of traditional inkjet printing, fluid surface energy constraints make it difficult for this technique to reach below the picoliter droplet size and 10 μm printed feature size regime without the use of additional patterning. Extrusion or filament-based 3D printing requires contact between the nozzle, extruded material, and substrate to facilitate printing. Without additional processing, this limits the printing resolution to the nozzle diameter or larger, depending on the material.[3,4] Using an applied electric field on polarizable fluids to get around energetic barriers to smaller droplet formation, electro-hydrodynamic inkjet printing (EHDIJ) is a noncontact printing technique that can produce directed femtoliter-size droplets from solution-borne functional materials with a wider range of viscosities than traditional, pressure-actuated inkjet printing. Coupled with optimally engineered materials, EHDIJ printing can provide many benefits over traditional micron-scale fabrication techniques including large-area photolithography, two-photon resist direct-write lithography, and electron beam lithography.[5,6] Here, a method is proposed for the direct deposition of high-refractive-index, functional optical materials to form meta-lens at mid-infrared wavelengths, demonstrating its effectiveness.

The meta-optic pattern for this project was developed using the principles of subwavelength diffractive optics. In this mechanism, the desired phase shift of the light is achieved by taking advantage of variations in the lateral size and orientation of the individual scatterers while maintaining a uniform thickness.[7]

back to content

METHODS

The printing solution is made from ethylene glycol (EG), titanium diisopropoxide bis(acetylacetonate) (75% in isopropyl alcohol, IPA), polyvinylpyrrolidone, PVP (≈55,000 mw), isopropyl alcohol, and poly(melamine-co-formaldehyde) methylated, a thermally induced crosslinking agent. The 1 mm × 1 mm meta-optical lenses are fabricated on an *n*-type silicon wafer. The substrate is coated with trichloro (1H, 1H, 2H, 2H-perfluorooctyl) silane, a hydrophobic self-assembling monolayer (SAM), to increase the contact angle of the printed solution. Under ambient conditions, the meta-surface was printed on the SAM-coated substrate, using an EHDIJ printer made by SIJ Technology. **Figure 1a,b** shows a schematic of the EHDIJ printer setup. **Figure 1c,d** shows the contact angle between the TiO_2 precursor printing solution and the Si substrate, with **Figure 1c** showing the ink on a clean Si wafer without the hydrophobic SAM and **Figure 1d** showing the contact angle on a clean Si wafer coated with the hydrophobic SAM. **Figure 1e** shows an example of the TiO_2 printing solution EHDIJ printed on an uncoated Si wafer and **Figure 1f** shows the same solution printed on the hydrophobic SAM-coated Si wafer. Both examples were printed using the continuous mode of the EHDIJ printer. The printer can also run in dropwise mode. The printer has stage movement control down to 1 µm.

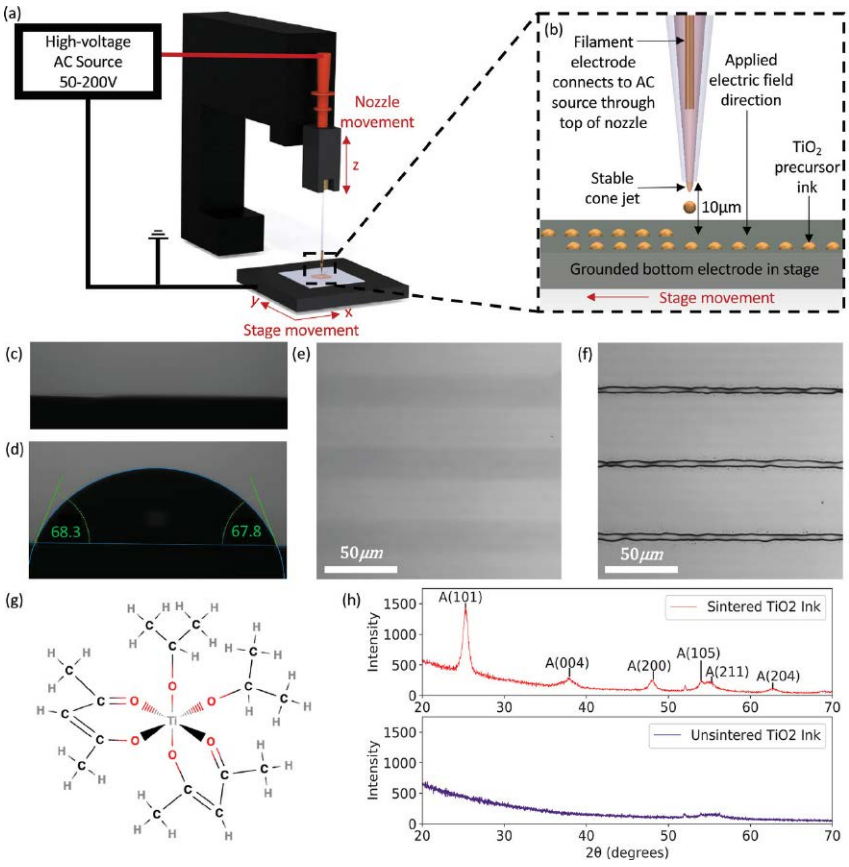

Figure 1: a) Wide-view schematic of EHDIJ printing setup. b) Close-up schematic of EHDIJ printing nozzle and substrate. c) Contact angle of TiO_2 precursor printing solution on clean Si substrate without the hydrophobic self-assembled monolayer coating to decrease droplet spreading and increase printing resolution. d) Contact angle of TiO_2 precursor printing solution on clean Si substrate with the hydrophobic self-assembled monolayer coating. e) EHDIJ printed TiO_2-PVP sink on Si wafer without the hydrophobic self-assembled monolayer coating. f) EHDIJ printed TiO_2-PVP sink on Si wafer with the hydrophobic self-assembled monolayer coating. g) Molecular diagram of TiO_2 precursor molecule. h) XRD of sintered (red) and non-sintered (blue) TiO_2 precursor ink.

The dropwise EHDIJ printing method uses point-by-point control of printing parameters. In this mode, the location and pitch of each drop are controlled by pausing droplet ejection during discrete stage movements before resuming ink flow at a defined location. The volume of the ejected drop is controlled by the parameters set at each point.

Mid-infrared meta-optical lenses were printed using the dropwise mode in four sequential patterns, coinciding with the four different diameters (1–4 µm) of the meta-atoms present in the optimal infrared lensing design. The printer nozzle was kept at a uniform height (≈10 µm) throughout the printing process. The alternating current was applied in a 75% square waveform, which was uniform across the entire print. Each printed pattern was made with a different applied bias and wave amplitude, to modulate the printed feature size following the pattern of the designed meta-optics lens. The individual features of each pattern were printed in a single printing pass under one set of parameters; larger features were not achieved by printing in the same location with multiple drops. This is achieved by increasing the applied voltage between the nozzle and the stage to increase the volume of the ejected drop.

Post printing, the sample undergoes a thermal conversion step to enable crosslinking of the PVP, evaporate the printing solvents, and convert the titania precursor to amorphous TiO_2. **Figure 1g** shows the molecular structure of the precursor titanium diisopropoxide bis(acetylacetonate). After the thermal crosslinking steps, the printed structures adhere

back to content

well to the polished Si substrate, as tested through scratch testing and sonication in a solvent bath. Selected samples were exposed to an additional sintering step to convert the amorphous TiO_2 into anatase and burn off the residual PVP. **Figure 1h** shows the X-ray diffraction (XRD) spectra of the TiO_2 printing solution before and after annealing.

RESULTS

Figure 2a shows an optical profilometry image and **Figure 2b** shows an SEM image of EHDIJ printed TiO_2 with an average feature diameter of 1.2 µm with a range of the printed features from 0.9 to 1.4 µm. The average height of the printed features in this array is 297 nm, as measured by AFM. This sample was printed using the continuous print mode with a printer bed speed of 2.0 mm s^{-1}. **Figure 2d** shows an optical profilometry image and **Figure 2**e shows an SEM image of EHDIJ printed TiO_2 printed using the dropwise print mode. This is an example of the range of features necessary to fabricate a meta-optics lens designed to focus 5 µm light. The different feature sizes present in this example are intentional and were printed using different applied biases and wave frequencies. The range of features in this example lies between 1.2 and 6.0 µm, as measured at the base of the printed feature. The designed range of sizes for the features was 1.0 to 4.0 µm. **Figure 2c,f** shows AFM height images of the samples from Figure 2a,d respectively. **Figure 2g** shows four AFM cross-sections of features with different base diameters (1.2, 2.2, 3.1, and 6.0 µm). The maximum height of each printed feature is 297, 597, 616, and 622 nm, respectively. The full width at half maximum of these printed features is 835 nm, 1.24 µm, 1.30 µm, and 3.6 µm, respectively.

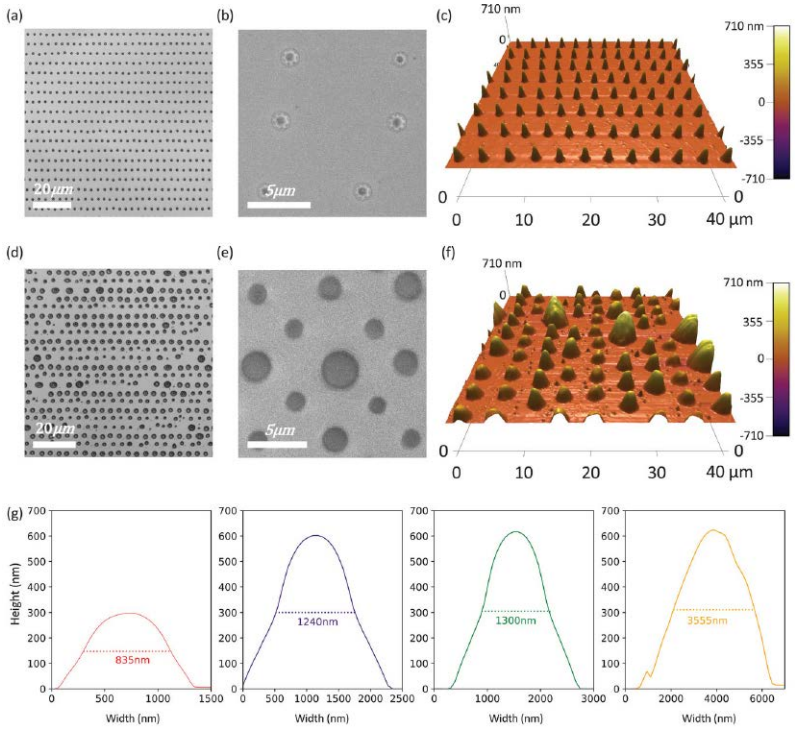

Figure 2: a) Optical profilometry image of TiO_2 precursor ink printed in continuous EHDIJ mode, the scale bar is 20 µm. b) SEM image of TiO_2 precursor ink printed in continuous EHDIJ mode, the scale bar is 5 µm. c) AFM height scan image of samples shown in (a). d) Optical profilometry image of TiO_2 precursor ink printed in dropwise mode using different printing parameters for differently sized features, the scale bar is 20 µm. e) SEM image of TiO_2 precursor ink printed in dropwise mode, the scale bar is 5 µm. f) AFM height scan image of samples shown in (d). g) Cross sections of printed features with four different sizes fabricated using different EHDIJ printing conditions showing the full width at half-maximum height of the features.

Once the materials, substrate surface, and EHDIJ printing processes were developed to provide droplet volume control and a lateral resolution of 1 µm for functional TiO_2, these techniques were applied to create a fully printed 1 × 1 mm mid-infrared meta-optics lens, based on discrete scattering features, designed to focus 5 µm light. The designed 2D meta-surface is made up of regions of features ranging from 1 to 4 µm in diameter with a 5 µm pitch between each feature, regardless of the feature diameter. The printed version of the meta-optics resulted in features ranging from 1.2 to 6.0 µm. The meta-surface was printed using the dropwise mode, and each feature was printed with a single drop of varying volume, rather than printing multiple drops of a uniform volume to increase feature size. The drop volume is varied by changing the applied bias between the nozzle tip and the stage. **Figure 3a** shows the as-designed meta-surface lens with each color in the pattern representing a different scattering feature diameter. **Figure 3b** shows a final, fully printed meta-optics lens, indicating that there is a high fidelity between the designed pattern and the printed pattern. Close-up images show that there are distinct diameter differences between the features printed at each set of printing parameters, with the larger features resulting from the higher voltage and larger wave amplitude. The 1 µm and 2 µm feature regions have consistently discrete features. The 3 and 4 µm feature regions have some discrete features but also show a significant number of merged structures. This defect appears to occur

back to content

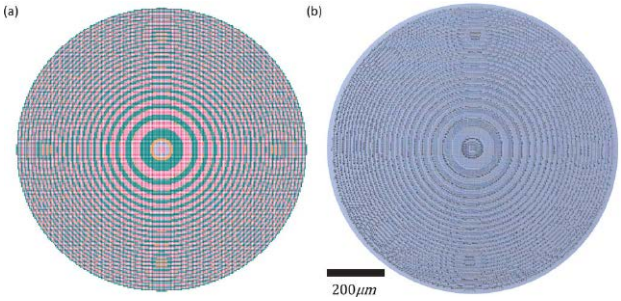

Figure 3:
a) Designed mid-infrared meta-surface lens. b) Optical profilometer image of fully printed mid-infrared meta-optics lens.

more frequently in regions of the substrate where there is a higher concentration of 3 or 4 μm diameter structures. There is a variation among the printed features of all diameters but because the feature-to-feature pitch is set at 5 μm in the mid-infrared meta-optics lens, as the features get larger, the room for error without resulting in merged printing drops decreases.

For the meta-lens shown in **Figure 3a,b,** the features designed to be 1 μm in diameter were printed with an applied voltage of 65 V, and the 2, 3, and 4 μm diameter features were printed with an applied voltage of 77, 95, and 105 V, respectively. However, other meta-lenses were printed in a range of 88–210 V for the 1–4 μm diameter features. This difference in absolute applied voltage is likely due to other variables in the printing setup, such as small variations in nozzle height. Increasing and decreasing the nozzle height has been shown to impact the voltage required to initiate ink jetting. The setup used for the EHDIJ printed meta-lenses allows for top-down control of the nozzle distance away from the substrate with a movement resolution of 1 μm. However, this is not a dynamically controlled printing parameter, and the nozzle height remains constant with respect to the top of the nozzle arm on the z-axis of the printer (see **Figure 1a**). Although these experiments were conducted in climate-controlled laboratory with HEPA-filtered airflows, it is also possible that small variations in temperature, ambient relative humidity, stage roughness, and substrate and ink handling could lead to variations in the electric fields required for a given printing outcome. Therefore, it can be reported that a positive correlation exists between the applied voltage and the resulting printed drop volume but a precise quantitative relationship is presently unknown.

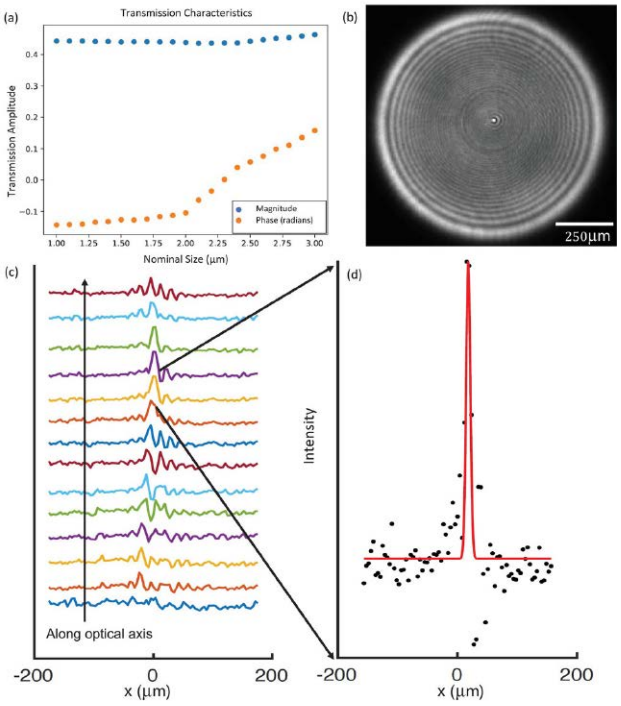

Figure 4: a) The amplitude and phase of the scatterer as a function of the scatterer diameter for light propagating perpendicular to the plane of the meta-surface that is typically parallel to the long axis of the scatter feature. b) Signal intensity image showing the most power in the focal spot at the center. c) Focusing measurements taken along the optical axis. d) Peak intensity focusing measurement showing FWHM of the beam spot is ≈15 μm.

To validate the fabrication method, we designed a meta-optical lens, under the constraints of the printing fabrication. The phase-distribution $\Phi(x, y)$ of the meta-lens with a focal length of f follows the hyperboloid phase profile:

$$\Phi(x,y) = 2\frac{\pi}{\lambda}\left(\sqrt{(x^2 + y^2 + f^2)} - f\right) \quad (1)$$

For printable photonics, the highest achievable thickness of the scatter is ≈1 μm, under the current materials and methods, which limits the phase-coverage. Under the constraints of the printable features, we estimated the phase coverage to be ≈ 0.6 π, which is sufficient to create a lens.[8] **Figure 4a** shows the amplitude and phase distribution of the designed meta-optics lens.

We characterized the printed meta-optics using a confocal microscopy setup in mid-IR. In this microscope configuration, a pulsed 5 μm quantum cascade laser (QCL) with 500 ns pulses, and repetition rate of 100 kHz is coupled to an InF_3 single-mode fiber (NA ≈0.26 with 9 μm core) and collimated using a black diamond

back to content

asphere (NA = 0.85) resulting in a collimated beam of ≈1 mm to match the meta-surface clear aperture. The meta-surface is translated relative to an imaging lens with a clear aperture of ≈25 mm and f = 12.7 mm. The image is captured on an InSb focal plane array (FPA) with a 15 µm pixel pitch and 640 × 512 pixels cooled to 76 K. The camera acquisition time is 0.9 ms to best fit the 14-bit dynamic range of the FPA and 100 frames are captured and averaged with background correction.

We observe the focusing of the light as we scan along the optical axis **(Figure 4c,d)** and we can fit the intensity at the focal plane to estimate the FWHM of the beam spot to be ≈15 µm. We note that the focusing behavior is sub-optimal due to low phase coverage but the focusing behavior is expected to improve as we expand our printing capabilities and print thicker materials.

DISCUSSION

TiO_2 precursor meta-surface printing trials for the 5 µm lens design revealed that the printing mode could significantly influence the printed feature resolution and feature shape. The highest resolution individually printed drops were consistently generated using continuous print mode.

The hydrophobic SAM used to coat the polished Si wafer is an essential process step to enable the high-resolution features achieved in this study. In terms of film thickness, this translates to an increase in the single drop height from 20 nm on the uncoated Si to as tall as 620 nm on the hydrophobic SAM-coated substrate. To optimally lens 5 µm light, the 1–4 µm diameter features should have a height of 1 µm. Lensing is still observable with a smaller feature height, but the results could be improved by printing higher aspect ratio features. One pathway to further increase feature height and aspect ratio is to use a different hydrophobic self-assembling monolayer as a surface treatment that results in a higher contact angle between the printing solution and substrate.

In addition to increasing the solution-substrate contact angle, the printed feature aspect ratio could be increased through the addition of TiO_2 nanoparticles to form a composite nanoparticle and precursor ink.[3] The nanoparticles could enable higher aspect ratio features compared to particle-free inks, as well as an increase in viscosity of the printing solution, which can lead to less lateral droplet spreading before the solvent loss and increasing viscosity effectively freezes the droplets at their maximum lateral dimensions.

The addition of TiO_2 nanoparticles could also lead to an increase in the refractive index of the printed features. There is a positive correlation between an increasing refractive index and a reduction in the focal length of the measured meta-surface lens, which is a device benefit for ultra-flat optics.[9]

The performance of the meta-surface is limited by the vertical height of the printable scatterer features, which limits the achievable phase coverage. Further increasing the aspect ratio of the printable film through ongoing ink materials, surface, and printing process parameter development will improve the phase coverage and efficiency.

CONCLUSION

In this study, a fully additive, maskless process for printing TiO_2 meta-surface lenses made with femtoliter dropwise control of the printed ink features was developed. This technique was used to create mid-IR optical meta-surface lenses that demonstrated focusing of 5 µm wavelength light. Two different EHDIJ printing modes, continuous and dropwise, were explored to create a minimum reproducible feature size of 1 µm. The dropwise method was used for the fully printed mid-infrared meta-surface lens, as it allowed for the greatest control over material deposition location and locally printed feature size. The reported results are the first of their kind both in the fields of printed meta-optics and EHDIJ printed ceramics.

EXPERIMENTAL SECTION

The printing solution was made by mixing PVP (0.625 g, 55000 Mw), EG (1.76 mL), and IPA (0.638 mL). The mix was stirred at room temperature (600 rpm, 2–3 h). Then, 1.1125 g of titanium diisopropoxide bis(acetylacetonate) (75 wt.% solution in IPA) and 0.125 g of poly(melamine-co-formaldehyde) methylated solution (≈84 wt.% in 1-butanol) were added to the solution. The solution was stirred at room temperature for 24 h. The final printing solution was made by taking 0.5 mL of the bulk solution and adding 0.5 mL of EG and

◀ back to content

0.5 mL of titanium diisopropoxide bis(acetylacetonate). This solution was mixed for 30 s using a vortex mixer at 2,000 rpm. Just before printing, the final solution was filtered using a 0.45 µm, water-wetting polytetrafluoroethylene (PTFE) membrane syringe filter.

The meta-optical lenses were fabricated on a double-side polished, n-type silicon wafer. The wafer was cleaned via sonication baths in deionized water with 10% detergent, pure DI water, acetone, and IPA. Then, the Si wafer undergoes a UV-ozone surface activation treatment for 10 min. Subsequently, the substrate was coated with trichloro(1H, 1H, 2H, 2H-perfluorooctyl)silane (97%). The hydrophobic coating was applied in an enclosed environment on a hotplate set to 125 °C (257 °F) for 2 h. After the application of the hydrophobic monolayer, the meta-surface was printed on the substrate. After printing the complete meta-surface, the substrate was placed on a 200 °C (392 °F) hotplate for 20 min. Some samples were heated in a box furnace to 450 °C (842 °F) and held at that temperature for 1 h. After the thermal conversion of the ink, the samples were assessed for printing quality.

REFERENCES

[1] *Arias, A.C., MacKenzie, J.D., McCulloch, I., Rivnay, J., and Salleo, A. (2010) Materials and Applications for Large Area Electronics: Solution-Based Approaches. Chem. Rev., 110 (1), 3–24.*

[2] *Burns, S.E., Kuhn, C., Jacobs, K., MacKenzie, J.D., Ramsdale, C., Arias, A.C., Watts, J., Etchells, M., Chalmers, K., Devine, P., Murton, N., Norval, S., King, J., Mills, J., Sirringhaus, H., and Friend, R.H. (2003) Printing of polymer thin-film transistors for active-matrix-display applications. J. Soc. Inf. Disp., 11 (4), 599.*

[3] *An, B.W., Kim, K., Lee, H., Kim, S.-Y., Shim, Y., Lee, D.-Y., Song, J.Y., and Park, J.-U. (2015) High-Resolution Printing of 3D Structures Using an Electrohydrodynamic Inkjet with Multiple Functional Inks. Adv. Mater., 27 (29), 4322–4328.*

[4] *Ahn, B.Y., Duoss, E.B., Motala, M.J., Guo, X., Park, S.-I., Xiong, Y., Yoon, J., Nuzzo, R.G., Rogers, J.A., and Lewis, J.A. (2009) Omnidirectional Printing of Flexible, Stretchable, and Spanning Silver Microelectrodes. Science (80-.)., 323 (5921), 1590–1593.*

[5] *Park, J.-U., Hardy, M., Kang, S.J., Barton, K., Adair, K., Mukhopadhyay, D. kishore, Lee, C.Y., Strano, M.S., Alleyne, A.G., Georgiadis, J.G., Ferreira, P.M., and Rogers, J.A. (2007) High-resolution electrohydrodynamic jet printing. Nat. Mater., 6 (10), 782–789.*

[6] *Zhang, B., He, J., Li, X., Xu, F., and Li, D. (2016) Micro/nanoscale electrohydrodynamic printing: from 2D to 3D. Nanoscale, 8 (34), 15376–15388.*

[7] *Huang, L., Colburn, S., Zhan, A., and Majumdar, A. (2022) Full-Color Metaoptical Imaging in Visible Light. Adv. Photonics Res., 3 (5), 2100265.*

[8] *Liu, C.-H., Zheng, J., Colburn, S., Fryett, T.K., Chen, Y., Xu, X., and Majumdar, A. (2018) Ultrathin van der Waals Metalenses. Nano Lett., 18 (11), 6961–6966.*

[9] *Bayati, E., Zhan, A., Colburn, S., Zhelyeznyakov, M.V., and Majumdar, A. (2019) Role of refractive index in metalens performance. Appl. Opt., 58 (6), 1460.*

◀ back to content

02 Designer glasses – future of photonic device platforms

Adapted from Fernandez *et al.* (2021)

INTRODUCTION

A tightly focused femtosecond laser can induce a localized and permanent refractive index change in a wide range of transparent dielectrics. Ultrafast laser inscription enables the creation of integrated photonics circuits providing true rapid prototyping functionality.

Glasses are often the substrates of choice. While they are easily accessible and have high optical quality, ultrafast laser inscription in these materials is often slow. Multicomponent silicate glasses, on the other hand, allow much faster inscriptions with ultrafast lasers at high repetition rates, but the optical quality of these glasses is often inadequate because they are contaminated with iron.

This work attempts to provide a complete picture of the dynamics and mechanisms of waveguide formation during high-repetition femtosecond laser irradiation by shedding light on why multicomponent glasses are so well suited for the ultrafast laser inscription process. Waveguide formation in four glass families (borosilicate, aluminosilicate, boro-aluminosilicate, and soda-lime silicate) using fourteen different commercial glasses was studied. Based on these results, an optimized glass composition was devised.

METHODOLOGY

All waveguides in this study were written using a 5.1 MHz high-repetition-rate Ti:sapphire chirped-pulse femtosecond oscillator laser emitting 50 fs pulses and operating at a wavelength of 800 nm. Circularly polarized laser pulses were focused inside the glass using an Olympus UPLANSAPO 100× oil immersion microscope objective (NA = 1.4). Waveguides were written at a depth of 170 µm using a set of 3-axis computer-controlled high-precision Aerotech air-bearing linear stages. The nominal composition of commercial glasses was determined using X-ray fluorescence (XRF) analysis.

All glasses were investigated under identical experimental conditions. Identical 30 µm diameter structures were inscribed in all glasses by adjusting the pulse energy for each feed rate.

The designer glasses were fabricated using the conventional melt-quench technique. The glasses were melted at a temperature of 1650 °C in platinum crucibles. Post waveguide inscription, the glass samples were cut to size and their end-face were ground and polished to optical quality. Images of the end-faces were recorded using an Olympus IX81 inverted optical microscope in differential interference contrast (DIC) mode. SEM imaging and electron probe microanalysis (EPMA) mapping of ion migration was carried out on a field-emission analyzer.

RESULTS

Ion migration in low aluminium and aluminium-free BK7 glass

Even though circular waveguides were formed, as shown in **Figure 1**, all the 30-µm diameter waveguides exhibited cracks around their periphery. Densified zones (positive index change) were found for >200 mm/min, whereas the first concentric ring had low density (negative index change). This behavior was reversed as soon as the feed rate dropped below 100 mm/min.

EPMA showed that the positive index core at a feed rate of 500 to 3,000 mm/min was mainly due to the migration of alkali. To our knowledge, this is the first report in which alkali forms a positive index core.

The inversion of migration directions of glass constituents for identical focusing conditions by just changing feed rate, as observed in BK7, challenges and adds new information to two existing theories on ion migration, which are 1) glass forming elements (silicon) migrate to

back to content

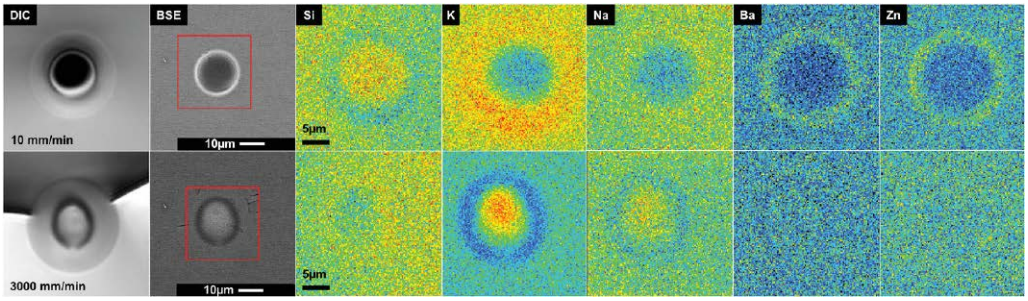

Figure 1: DIC, backscattered electron image (BSE), and elemental maps of BK7 waveguides written with 10 mm/min (first row) and 3,000 mm/min (second row) feed rates. The rainbow color scale for the elemental maps ranges from blue to red indicating low to high concentration.

the focal point (highest temperature) and 2) SiO_2 migrates to hot (cold) side in SiO_2-rich (poor) compositions due to an existing negative (positive) Soret coefficient and the reversal of the trend happened around 20 mol%.

ION MIGRATIONS IN ALUMINIUM-RICH SILICATE GLASSES

Alkali rich glasses

For alkali-rich glasses, Asahi Dragontrail, Corning Gorilla-3, and Schott Xensation-3D glasses were selected. The backscattered electron (BSE) images of structures written between 200–3,000 mm/min revealed a core that has a complex combination of high and low-density zones despite featuring an exclusive positive refractive index contrast.

For the alkali-rich but alkaline earth-deficient glasses Gorilla 3 and Xensation 3D, the positive index core produced at high feed rates was primarily associated with a change in polarizability due to non-bridging oxygen (NBOs) atoms. Dragontrail's composition was relatively rich in alkaline earth, which resulted in a densified high index core through the accumulation of alkaline earth albeit with a low index contrast. Alkali and alkaline earth are both glass modifiers.

Alkali-free, alkaline earth boro-aluminosilicate glasses

The morphology of high-alkaline-earth-containing glasses with relatively low aluminium concentrations, such as high-barium 7059F and AF45, stood out from other high-alkaline-earth-content glasses. These glasses exhibited a vertically elongated, inhomogeneous core. Enrichment of alkaline earth elements in the core was common to all alkaline earth glasses, resulting in densification and an increased refractive index, while silicon migration to the low-index and low-density regions surrounding the positive-index core was observed.

Key factors for sustaining a positive index core with circular morphology

Aluminium tends to migrate towards densified zones in peraluminous glass compositions. For the alkaline earth boro-aluminosilicate glasses, a non-circular waveguide core was observed for AF45 and 7059F, whose Al:[AE+Alk] ratios are 0.376 and 0.4, respectively. Aluminium reverses its trend in these peralkaline compositions, where it migrates to low-density zones and is no longer a refractive index provider for wave guidance.

Dragontrail, Gorilla 3, and Xensation 3D glasses have ratios of 0.215, 0.405, and 0.41, respectively. The main physical property that is influenced by the Al:[AE + Alk] ratio is a sharp change in viscosity. The viscosity is at its maximum when the Al:[AE + Alk] molar ratio is 0.5, where there is a perfect balance between Al and charge-compensating modifiers.

When the composition is in the peralkaline domain, the waveguide-forming region undergoes a sharp decrease in viscosity with high gradients owing to the segregated migration of element species. However, there was only a minor variation in the viscosity of the peraluminous composition. It could be that the former situation causes waveguide formation in Gorilla 3 and Xensation 3D in a more unpredictable fashion, depending on where aluminium migrates to. It is known that lowering the SiO_2 content reduces the viscosity of the glass melt at a particular temperature. Hence, during laser inscription, strong viscosity gradients owing to peralkaline compositions at lower viscosities produce highly asymmetric waveguide morphologies in AF45 and 7059F.

back to content

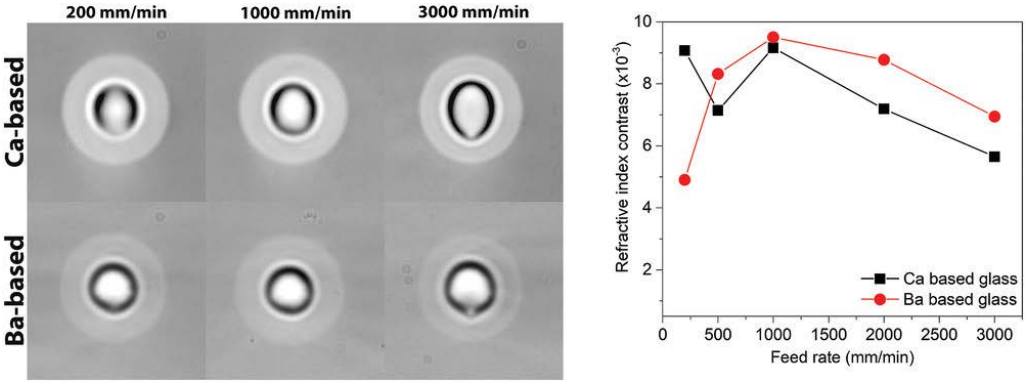

Figure 2: a) DIC images of the 30 µm sodium-aluminosilicate glass waveguides with the addition of calcium (1st row) and barium (2nd row). The waveguides were written at feed rates of 200 (1st column), 1,000 (2nd column), and 3,000 (3rd column) mm/min. (b) Refractive index contrast as a function of feed rate.

It was determined that the presence of aluminium in alkaline-earth boro-aluminosilicate glasses prevented the depletion of calcium and other alkaline earth elements in the core, possibly because of the additional role of Al as a charge compensator.

Designer glass

The following formula (all in wt. %) for alkali-alkaline earth aluminosilicate glass was proposed:

$(100-(1+a_1+b_1)\cdot x)\ SiO_2\cdot(x)$
$Al_2O_3\cdot(a_1\cdot x)MO\cdot(b_1\cdot x)\ R_2O$

Where MO is the alkaline earth metal oxide and R_2O is the alkali metal oxide. The preferred composition of Al_2O_3 was selected to be between x = 15–25 wt%. Two different compositions were prepared, based on calcium and barium. The composition of the glass was $57SiO_2$-$25Al_2O_3$-$9Na_2O$-9MO where M was replaced by Ca and Ba. Glasses were fabricated using the conventional melt-quenching technique. The 30 µm structures were fabricated within these glasses, and the morphological effect of an increase in the Al:[AE+Alk] ratio value was observed in the DIC image (**Figure 2**) as the composition from lighter Ca to heavier Ba was changed. The barium-based glass exhibited a more circular morphology within the same inscription window as compared to the keyhole morphologies of AF45 and 7059F.

CONCLUSION

The aluminium to alkaline earth + alkali ratio was found to be the prime parameter controlling the formation of circular and positive index waveguide cores. Aluminium, the sole glass intermediate in all of the silicate glasses investigated in this study, was found to assume the role of a glass former in peraluminous glass compositions, which tends to migrate towards the densified/positive index core exhibiting a contrary behavior in peralkaline compositions. Aluminium was also found to be the key element for maintaining a positive-index core and waveguide circularity. The results further show that the presence of alkaline earth elements as well as the addition of alkalis triggers densification in the core region. Heavier alkaline earth promotes an increase in the refractive index while ensuring that a peraluminous glass composition helps the waveguide core to maintain the desired circular morphology.

back to content

03 Ultrafast coherent spectroscopy of a GaAs quantum dot

Adapted from Wolpert *et al.* (2012)

The controlled interaction of several quantum dots (QDs) mediated by plasmonic or photonic nanostructures promises interesting new functionality in the fields of quantum computing and telecommunication. The focus of this article is on the technique of transient reflection spectroscopy, which can be applied to a broad range of samples and devices. This article demonstrates the versatility of the approach by presenting several quantum optical studies such as Rabi oscillations, perturbed free induction decay, and quantum beats from an entangled excitonic state in weakly absorbing GaAs QDs. The experimental setup includes an Olympus microscope objective (LCD Plan FL N) that can be used to examine individual quantum dots at densities of less than 1 dot/μm^2.

INTRODUCTION

In recent years substantial efforts were made to produce matter quantum bits (standing qubits) in various systems.[1] These quantum mechanical two-level systems can be realized by atom-like systems such as single molecules, nitrogen-vacancy centers in diamonds, or semiconductor quantum dots (QDs).

Semiconductor QDs are appealing systems in this context as they are pure solid-state systems which makes them stable, long-lived, and compatible with conventional 2D fabrication techniques.

In this feature article, the focus is on the demanding task of coherent spectroscopy in complex quantum systems. One needs a non-invasive optical technique that does not interfere with the structure around the QD. Optical far-field spectroscopy is a technique that complies very well with these terms.

TRANSIENT DIFFERENTIAL REFLECTION SPECTROSCOPY OF SINGLE QUANTUM DOTS

The method is based on the optical theorem, [2] which states that absorption and scattering of light by a dipole can be understood on the same footing. One can detect absorption in the transmitted light by the interference of the light scattered by the dipole with the light passing it unperturbed. The same interference can be exploited in reflection.

back to content

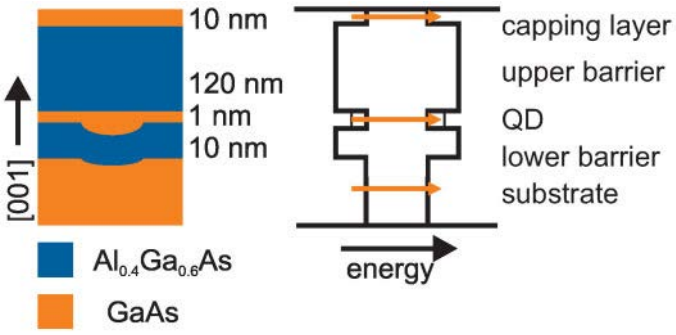

Figure 1: Left: Epitaxial grown layered structure of the quantum dot sample. Right: Simplified band edge diagram of the structure in the growth direction. Substrate and capping layer are absorbing light at the s-shell exciton resonance.

The spectral shape of the detected light is directly influenced by the phase lag due to interference. Starting from an absorption dip at zero phase lag, the spectral shape of the signal gradually gets dispersive when reaching a phase lag of $\varphi = \pi/4$. Between these values, the shape is a mixture of both and the signal usually appears as an asymmetric dispersive line.[3] This technique will be applied to ultrafast spectroscopy of a weakly absorbing self-assembled QD.

SAMPLE

The quantum emitters are epitaxial GaAs QDs in AlGaAs barriers.[4] In detail, samples were grown by a solid-source molecular-beam epitaxy (MBE) machine equipped with an $AsBr_3$ gas etching unit. As a first step, a layer of self-assembled InAs QDs was grown on the GaAs substrate on a (001)-surface. The nominal substrate temperature was 500 °C (932 °F). Then, a 10 nm GaAs layer was grown on top of the InAs QDs. As a result of the strain-enhanced and material-selective etching rate, bow-tie-shaped nanoholes were created by removing the buried InAs QDs by in situ nominal 5-nm-deep $AsBr_3$ etching. The formed nanoholes were overgrown with 10 nm $Al_{0.45}Ga_{0.55}As$, which serves as the lower barrier of the potential well. For moderate barrier thickness, the nanoholes are preserved due to the low mobility of the AlGaAs. As the next step, GaAs were deposited as the lower band gap material. To close the holes completely by diffusion, the sample was kept at a temperature of 500 °C (932 °F) for 1 min. This results in a plane and smooth GaAs surface. Then the upper barrier layer of $Al_{0.45}Ga_{0.55}As$ was grown and in the last step, a GaAs capping layer is deposited to achieve passivation and chemical stability. The structure is drawn schematically on the left of **Figure 1.** The right part of the **Figure** shows a simplified band edge diagram.

The spatial asymmetry of the QD leads to linear polarization selection rules and a fine structure splitting (FSS) in the order of 100 µeV between the two fundamental bright exciton states.[5] Although the biexciton emission is polarization dependent, the level is not by itself split. It is a consequence of the FSS of the excitons. The trion lines appear as straight lines as they are not split. The polarization directions, P_{90} and P_0, are oriented along the crystal axes [1$\bar{1}$0] and [110].

EXPERIMENT

Transient differential reflection spectra were acquired by measuring the spectrum of reflected probe pulses alternating with and without applying a pump pulse. The setup is depicted in **Figure 2.** Orthogonally polarized pump and probe pulses were derived from a mode-locked Ti:Sapphire laser with a pulse duration of 150 fs at a wavelength of 720 nm and a repetition rate of 76 MHz. After cutting out sub spectra using a grating pulse shaper[6] the pulses had a duration of about 1ps and a spectral width of 4 meV. The pump pulses were delayed by a time Δt with respect to the probe pulses using a mechanical delay stage before the two beams were recombined again by a polarizing beam splitter. Pump and probe pulses were focused on the

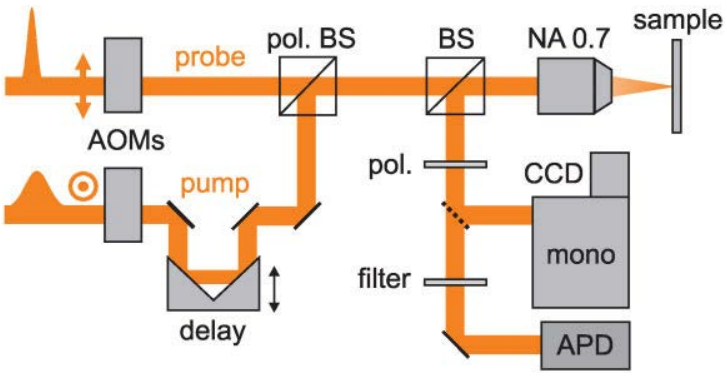

Figure 2: Schematic overview of the setup employed to measure transient reflection spectra of single quantum dots.

back to content

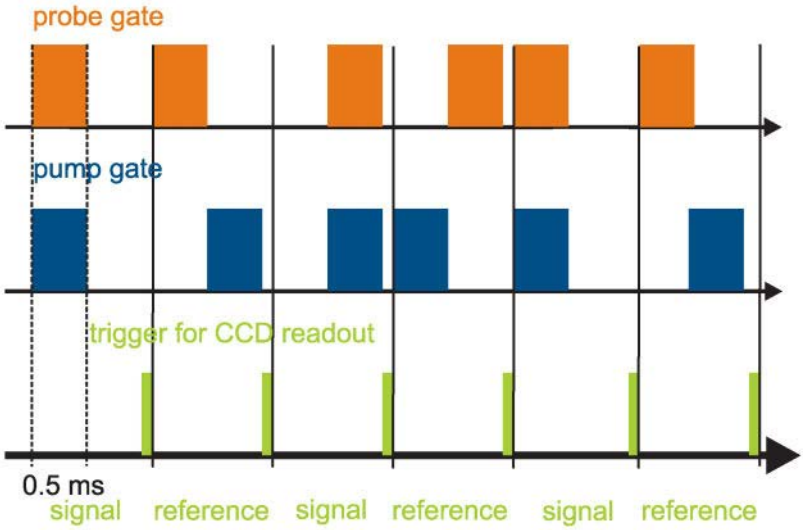

Figure 3: Gating scheme: Signal and reference frames are alternatingly recorded. For a signal spectrum, both pump and probe beams are gated on at the same time by the AOMs, whereas they are displaced in time for a reference spectrum. Short trigger pulses are fed to the CCD controller so that the readout is always synchronous with the AOM gating signals.

sample down to a spot of 750 nm in diameter by a microscope objective with a numerical aperture of 0.7 (Olympus, LCDPlanFL N) and a magnification of 50. The sample was mounted in a cryostat at a temperature of T = 10 K.

The spatial resolution of the microscope allowed us to address single QDs at densities of less than 1 dot/mm^2. Reflected light from the sample was collected with the same objective again. After passing a beam splitter the pump light was efficiently suppressed by a combination of a Soleil–Babinet compensator and a Glan–Thompson polarizer. The orthogonally polarized probe light was coupled into a spectrometer with 1,800 grooves/mm reflective grating and detected by a back-illuminated deep-depletion charge-coupled device camera. Rapid readout allowed us to acquire spectra at a rate of 1 kHz.

Differential reflectivity spectra $\Delta R/R$ of a single QD were acquired by taking the difference of the probe reflection spectra with and without preparing an excited state by the pump pulse. Pump and probe beams were switched on and off independently by acousto-optic modulators (AOMs) on a millisecond timescale. To reduce the acquisition time an area of only 400 × 20 pixels directly under the readout register was illuminated and read out. A double modulation scheme was employed to remove the effect of residual pump light that reaches the CCD chip, despite the suppression by polarizing optics. **Figure 3** gives an overview of the AOM gating and the timing of the experiment. For all spectra, the opening time of the pump and the probe AOM were the same. The same amount of residual pump light always reached the camera. The difference between signal and reference spectra is that in signal spectra the pump and probe beams are active simultaneously. In reference spectra, the active phase is shifted by 0.5 ms. As the excitations in the sample are short-lived compared to the displacement of the pump and probe gating windows, there is no pump-induced signal in a reference spectrum. To minimize effects from loss of charge in the CCD pixels between exposure and readout the order of pump and probe gating windows is interchanged. A dataset of signal and reference spectra modulated at 1 kHz was thus obtained. $\Delta R/R$ spectra are obtained by subtracting the sum of the odd from the sum of the even frames. An integration time of ten minutes gives, for example, 4×10^5 spectra which had about 1×10^4 photons incident on each pixel. This results in about 5×10^{10} collected photons making shot-noise-limited measurements of signals as small as 4×10^{-6} possible.

back to content

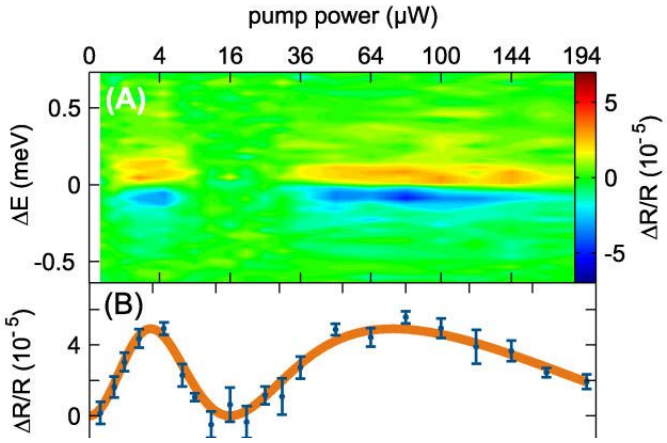

Figure 4: (A) Each vertical cut through the color map represents a ΔR/R spectrum at a given pump power and a fixed pump–probe delay Δt = 150 ps. The broad background has been subtracted. (B) By fitting the dispersive line shape function to the spectra in (A), the signal amplitude (blue dots) is extracted. The error bars are the standard deviation of four consecutive measurements. The scale of the pump pulse area θ_P is calibrated to the first maximum. The data can be described by $\sin^2(\theta)$, considering an effective, reduced pulse area θ_{eff} due to delocalized carriers around the quantum dot (red curve). Figure adapted from Reference 7.

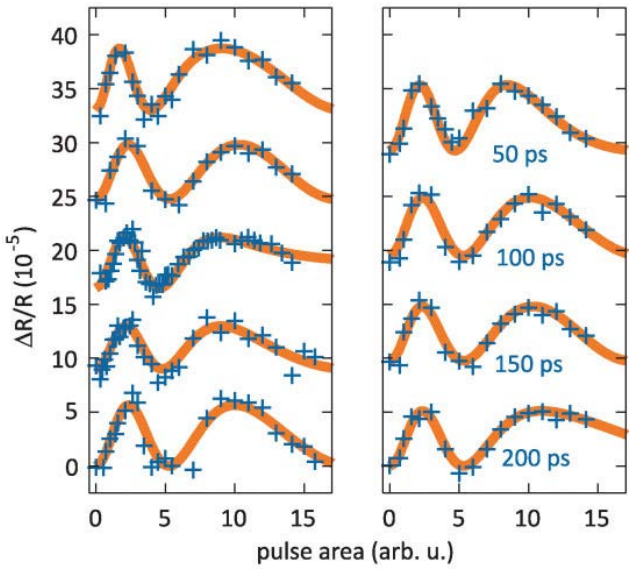

Figure 5: Left: Rabi oscillations measured on different QDs at Δt = 150 ps. Right: Rabi oscillations in one QD (A4) at different pump–probe delays.

RABI OSCILLATIONS IN A QUANTUM DOT ON AN ABSORBING SUBSTRATE

If the QD is excited with a laser pulse much shorter than its coherence decay time, the formed excitonic state and the light field stay coherent during the interaction. This leads to the well-known Rabi flopping between the two states of the $|00\rangle \rightarrow |10\rangle$ transition.

If the $|10\rangle$ state is populated by the pump pulse, the $|00\rangle \rightarrow |10\rangle$ transition will bleach to some extent. The spectral signature of bleaching is shown in **Figure 4A.** Here, every vertical line is a ΔR/R spectrum at a certain pump power. The signal reaches a maximum around a pump power of 3.5 μW corresponding to a π-pulse. The signal vanishes at a power of θ_P =15 μW, corresponding to a 2π-pulse. A dispersive line shape is to be used as a fitting function to extract the signal amplitudes, shown in **Figure 4B.** Two complete cycles of the Rabi oscillation are visible. They show, in contrast to textbook examples, a gradual stretching of the oscillation period.[7]

Rabi oscillations were measured on several QDs with pump–probe delays varying between 50 and 200 ps. **Figure 5** shows results for different QDs on the left and for different delay times on the right-hand side. All datasets were fit with an effective pulse area model [8] so that saturation parameters as well as dipole moments could be determined.

In summary, saturation intensities of the GaAs photocarriers were obtained between 150 and 600 MW/cm^2 which agrees well with the values given by the literature. The broad range of values of a fitting parameter f [8] suggests that the environment of the QDs is not uniform. The defect density of the substrate near the QD plays a crucial role in saturation effects. Moreover, it is thought that the fabrication process involving partial overgrowth and etching of sacrificial InAs QDs gives rise to very heterogeneous environments of the GaAs QDs on the sample. On the other hand, the transition dipole moments of all investigated dots lie within 17 and 19 Debye, apparently unaffected by changes in the environment. This underlines the power of optical spectroscopy when it comes to single nano-objects.

◀ back to content

PERTURBED FREE INDUCTION DECAY

The dynamics of the excitonic states were now considered. A famous example is the perturbation of the free induction decay by a short laser pulse.[9–11] In this experiment, the probe pulse created a coherent superposition of the crystal ground state and one of the excitonic states, e.g., $|00\rangle \rightarrow |10\rangle$, which gave rise to polarization. After the polarization was created by the probe pulse, it evolved freely and decayed exponentially with the coherence dephasing time due to elastic interaction with the environment. This corresponded to the loss of coherence between the states such that only a statistical mixture of the ground state and the exited state remained. The Fourier transform of the polarization time trace corresponded to the absorption spectrum. An exponential decay in time will result in a Lorentzian spectral line. The decay of the polarization may be disturbed by a second light pulse which gives rise to additional spectral features. Thus, conclusions were drawn about the dynamics of the system by merely investigating the transient spectral response.

The results of such an experiment are shown in **Figure 6A**. The pump pulse was polarized to drive the $|00\rangle \rightarrow |10\rangle$ transition while the probe polarization was adjusted to the $|00\rangle \rightarrow |01\rangle$ transition. At positive delays (pump arriving first) the signature of ground state bleaching caused by the pump pulse can be identified in the spectrum. At negative delays (probe arriving first) spectral oscillations were observed that indicate the perturbation of the polarization decay. The frequency of these oscillations increases with increasing pump–probe delay.

SPECTRAL FRINGES

The frequency of the spectral oscillations at negative delay is a function of the pump–probe delay. This can be understood easily: in **Figures 6E** and **F** the simulated temporal evolution of the polarization of the probed transition is shown, once for positive and once for negative pump–probe delay. In both figures, the red curve shows the polarization decay with the pump pulse while the blue curve shows the free induction decay without the pump pulse. The Fourier transform of their difference yields the differential reflectivity spectra shown in **Figure 6B.** When the delay is positive and the pump pulse comes first, the polarization induced by the probe pulse decays freely and the normal ground state bleaching signal appears. When the delay is negative and the probe pulse comes first, the probe-induced polarization is perturbed by the following pump pulse. More precisely, the pump

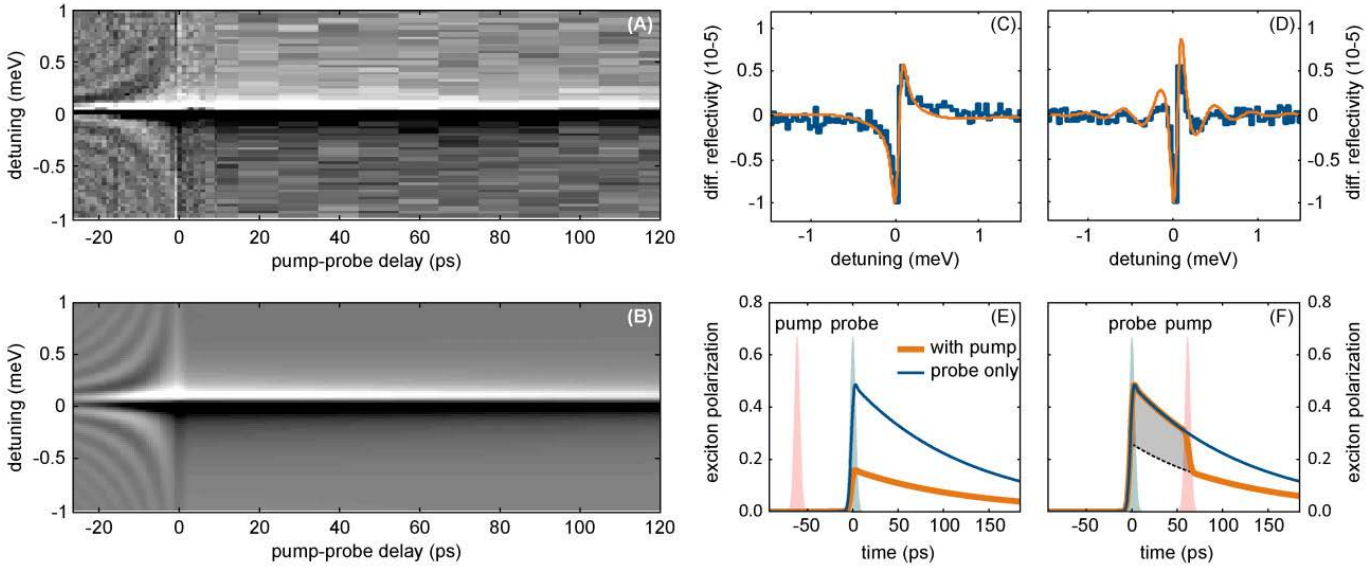

Figure 6: (A) Measured spectral map of a delay scan. Negative delay means that the probe pulse comes first. (B) Numerical simulation of the experiment using a 3-level density matrix approach. (C and D) Cuts of the spectral maps along the energy axis for measured data (blue curve) and simulated data (red curve) in the case of (C) positive delay and (D) negative delay. (E and F) Time trace of the polarization of the probed transition in the case of (E) positive delay and (F) negative delay. Figure adapted from Reference 7.

back to content

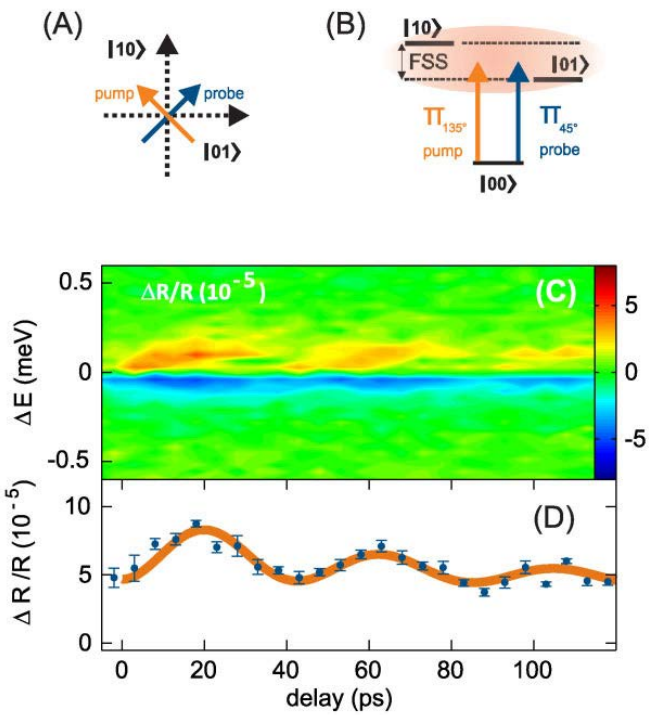

Figure 7: Raw data of the ΔR/R spectra as a function of pump–probe delay. Signal amplitudes of the excitonic state (blue dots in (D)) have been extracted from the spectral data (C) by a least square fit assuming two transition lines with a difference in energy equal to the FSS (sketched in (B)). We can identify the population decay with a time constant Tpop superimposed with quantum beats having a damping time T_{Raman}.

pulse promotes population from the crystal ground state into the |10⟩ state, which decreases the probe-induced polarization between the crystal ground state and the |01⟩ state. The resulting polarization trace can be seen as the sum of the normal exponential decay and a rectangle with a width equal to the pump–probe delay. This is indicated by the shaded area in **Figure 6F.** It is the Fourier transform of the rectangle (a sinc-function) that produces the oscillations in the spectra. The frequency of the oscillation is proportional to the length of the rectangle and thus proportional to the pump–probe delay. It does not depend on other parameters such as pulse area, dephasing time, or lifetime. As in the presented Rabi oscillations, this example shows again that the great advantage of spectrally resolved experiments is that one can distinguish between different contributions to the overall signal such as background contributions, coherent artifacts, and bleaching due to their different spectral characteristics.

QUANTUM BEATS IN A TWO EXCITON SYSTEM

Until now the pump pulses created a coherent superposition of the ground state |00⟩ and the exciton state |10⟩. By rotating the polarization of the pump beam by 45° (see **Figure 7A**) a coherent superposition of the two bright exciton states $\alpha|10\rangle - \beta|01\rangle$ can be created (see **Figure 7B**), the so-called Raman coherence.[11] As the transition energies differ by the FSS the resulting state will exhibit a beating with just this frequency difference. The evolving superposition state was probed with an orthogonally polarized probe pulse as a function of the pump–probe delay Δt. The excitation and readout process can be described in terms of quantum-mechanical superpositions and projections. In the following, the population that is left by the pump pulse in the ground state |00⟩ was neglected for simplicity. The population in the biexciton state |11⟩ was also neglected as the biexciton binding energy (6 meV) was large enough to bring the exciton–biexciton transition out of the resonance superposition state with the pump laser. At a time t=0, an entangled superposition state $|\psi(0)\rangle = |-\rangle = 1/\sqrt{2}\,(|10\rangle - |01\rangle)$ was created. The state evolves in time as:

$$|\psi(t)\rangle = 1/\sqrt{2}\,(e^{i\omega_1 t}|10\rangle - e^{i\omega_1 t}|01\rangle) \quad (1)$$

$$= 1/\sqrt{2}\,e^{i\omega_1 t}|10\rangle - e^{i\omega_{12} t}|01\rangle) \quad (2)$$

where $\omega_{1,2}$ are the angular frequencies of the two excitonic transitions and ω_{12} is their difference frequency.

After the pump–probe delay time Δt the polarization of the excited dipole along the polarization axis of the probe pulses was probed, which corresponds to a state

$|+\rangle = 1/\sqrt{2}\,(|10\rangle + |01\rangle)$ in the exciton basis. The probe projects $|\psi(t)\rangle$ onto $|+\rangle$. The probability of finding $|\psi(t)\rangle$ in the probe polarization direction is:

$$|\langle\psi(\Delta t)|+\rangle|^2 = \langle\psi(\Delta t)|+\rangle\langle+|\psi(\Delta t)\rangle \quad (3)$$

$$= (1 - e^{-i\omega_{-12}\Delta t})\,\frac{1}{4}\,(1 - e^{-i\omega_{12}\Delta t}) \quad (4)$$

$$= (1 - e^{-i\omega_{-12}\Delta t})\,\frac{1}{2}\,\cos(\omega_{12}\Delta t) \quad (5)$$

Thus, a $(1\text{-}\cos(\omega_{12}\Delta t)/2)$ beating in a series of transient reflectivity spectra when varying the pump–probe delay Δt is expected.

◀ back to content

For the experimental realization, both pump and probe pulses were adjusted to a pulse area of π/2. The transient ΔR/R spectra shown as a spectral map in **Figure 7C** reveal three quantum beats. The two overlapping spectral signatures of both excitonic transitions were fit by two equally strong lines at a fixed separation. The amplitude of this spectral signature is obtained for each pump–probe delay Δt and depicted in **Figure 7D.** It in turn can be fitted by assuming that only in a part of the ensemble a coherent superposition was reached. This part shows the beating that decays with a characteristic Raman coherence time T_{Raman}. The rest of the ensemble was just excited either to $|10\rangle$ or $|01\rangle$, followed by a population decay with a time-constant T_{pop}. The sum of both yields the signal:

$$\Delta R/R = a e^{-\frac{\Delta t}{T_{pop}}} + b\,(1 - cos\,(\omega_{12}\,\Delta t)/2)\, e^{-\Delta t/T_{Raman}} \quad (6)$$

The amplitudes extracted from the ΔR/R spectra are described very well by this model, as can be seen by the good agreement of the data points and the least square fit (red line in **Figure 7D**). T_{pop} = 230ps and T_{Raman} = 90 ps. The beating period corresponds to $\hbar\omega_{12}$ = 96 μeV which is very close to the FSS of 97 μeV determined by photoluminescence. From the Raman coherence time, T_{Raman} and the population decay time T_{pop}[12] the pure dephasing time of the coherent polarization was calculated to be about 150 ps.

SUMMARY

Transient reflection spectroscopy is demonstrated to be a versatile tool for the preparation and readout of solid-state-based single quantum systems. The only prerequisite for the technique is optical access to the quantum system from one direction. An arbitrary population state can be prepared and read out by driving Rabi oscillations in the neutral exciton transition of a GaAs QD. Having access to multichannel spectroscopic information allowed the explanation of deviations from the behavior of a simple two-level system. The interaction between hot delocalized carriers and the exciton confined in the QD was taken into account to describe the experimental data. In a separate experiment perturbed free induction decay of a localized exciton could be fully described by a three-level system involving the crystal ground state and the two single exciton transitions in the QD. Due to sensitivity to the coherent polarization in the sample, quantum beats from an entangled superposition state of the two fine-structure split exciton states were recorded straightforwardly. From these measurements, a Raman coherence time of 90 ps and a pure dephasing time of 150 ps were determined.

REFERENCES

[1] *Bennett, C.H., and DiVincenzo, D.P. (2000) Quantum information and computation. Nature, 404 (6775), 247–255.*
[2] *Jackson, J.D., and Fox, R.F. (1999) Classical Electrodynamics, 3rd ed . Am. J. Phys., 67 (9), 841–842.*
[3] *Karrai, K., and J. Warburton, R. (2003) Optical transmission and reflection spectroscopy of single quantum dots. Superlattices Microstruct., 33 (5–6), 311–337.*
[4] *Rastelli, A., Stufler, S., Schliwa, A., Songmuang, R., Manzano, C., Costantini, G., Kern, K., Zrenner, A., Bimberg, D., and Schmidt, O.G. (2004) Hierarchical Self-Assembly of GaAs/AlGaAs Quantum Dots. Phys. Rev. Lett., 92 (16), 166104.*
[5] *Plumhof, J.D., Křápek, V., Wang, L., Schliwa, A., Bimberg, D., Rastelli, A., and Schmidt, O.G. (2010) Experimental investigation and modeling of the fine structure splitting of neutral excitons in strain-free GaAs/AlxGa1-xAs quantum dots. Phys. Rev. B, 81 (12), 121309.*
[6] *Postma, S., van der Walle, P., Offerhaus, H.L., and van Hulst, N.F. (2005) Compact high-resolution spectral phase shaper. Rev. Sci. Instrum., 76 (12), 123105.*
[7] *Wolpert, C., Dicken, C., Atkinson, P., Wang, L., Rastelli, A., Schmidt, O.G., Giessen, H., and Lippitz, M. (2012) Transient Reflection: A Versatile Technique for Ultrafast Spectroscopy of a Single Quantum Dot in Complex Environments. Nano Lett., 12 (1), 453–457.*
[8] *Wolpert, C., Dicken, C., Wang, L., Atkinson, P., Rastelli, A., Schmidt, O.G., Giessen, H., and Lippitz, M. (2012) Ultrafast coherent spectroscopy of a single self-assembled quantum dot. Phys. status solidi, 249 (4), 721–730.*
[9] *Fluegel, B., Peyghambarian, N., Olbright, G., Lindberg, M., Koch, S.W., Joffre, M., Hulin, D., Migus, A., and Antonetti, A. (1987) Femtosecond Studies of Coherent Transients in Semiconductors. Phys. Rev. Lett., 59 (22), 2588–2591.*
[10] *Joffre, M., la Guillaume, C.B. à, Peyghambarian, N., Lindberg, M., Hulin, D., Migus, A., Koch, S.W., and Antonetti, A. (1988) Coherent effects in pump–probe spectroscopy of excitons. Opt. Lett., 13 (4), 276.*
[11] *Guenther, T., Lienau, C., Elsaesser, T., Glanemann, M., Axt, V.M., Kuhn, T., Eshlaghi, S., and Wieck, A.D. (2002) Coherent Nonlinear Optical Response of Single Quantum Dots Studied by Ultrafast Near-Field Spectroscopy. Phys. Rev. Lett., 89 (5), 057401.*
[12] *Li, X., Wu, Y., Steel, D., Gammon, D., and Sham, L. (2004) Raman coherence beats from the entangled state involving polarized excitons in single quantum dots. Phys. Rev. B, 70 (19), 195330.*

◀ back to content

04 Surface detection filter for transparent film OLS50-QWP

If the transparent film is laminated on the sample top surface, OLS5100 detects the boundary surface with the highest reflected light intensity among boundary surfaces of the transparent film. Since the reflected light intensity is determined by the film materials, base materials or top surface conditions, OLS5100 may not detect the intended boundary surface necessarily. The surface detection filter is an optical element to polarize the balance of the reflected light intensity among multiple boundary surfaces using the feature of polarization. Using the surface detection filter may detect the boundary surface you desire in some cases.

TIP

You may not detect the boundary surface with the following sample:

- Sample where the distance between boundary surfaces is short
- Sample where the reflectivity of the boundary surface is extremely different

USES OF THE FILTER | USE 1

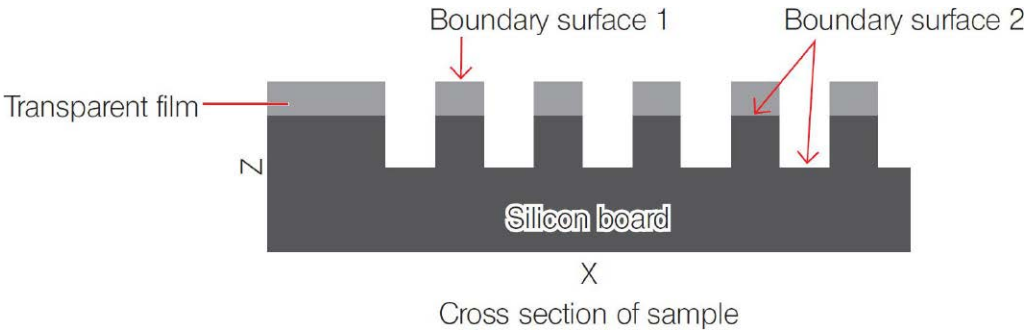

Cross section of sample

back to content

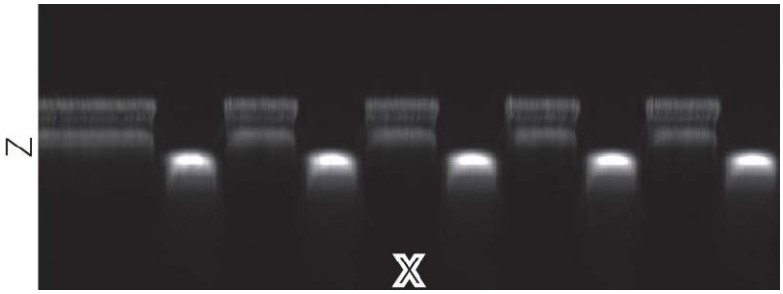

Reflected light intensity (when the filter is not used)

When the filter is not used

Since the reflected light intensity on the top surface and the bottom surface of the transparent film are almost same, the boundary surface 1 and the boundary surface 2 are detected in mixed status.

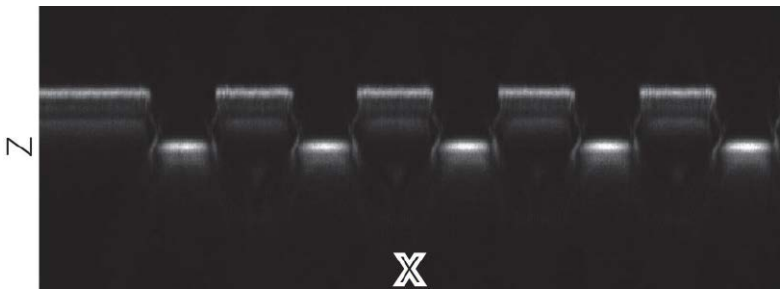

Reflected light intensity (when the filter is used)

When the filter is used

The reflected light intensity on the top surface of the transparent film becomes stronger and the top surface shape of the topmost layer of the sample is detected.

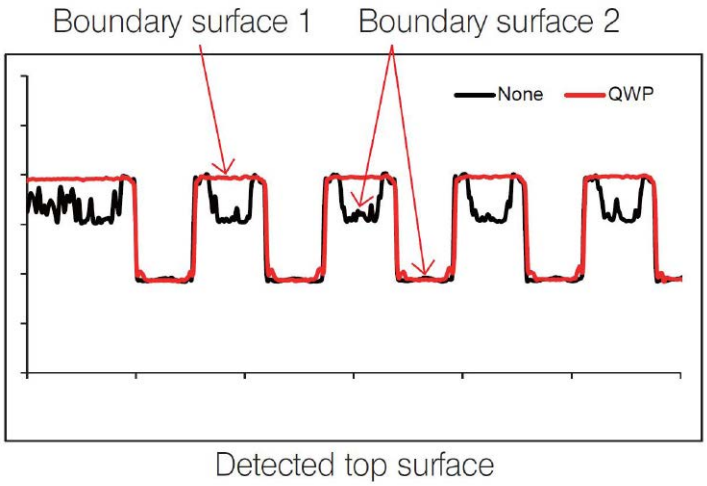

back to content

USES OF THE FILTER | USE 2

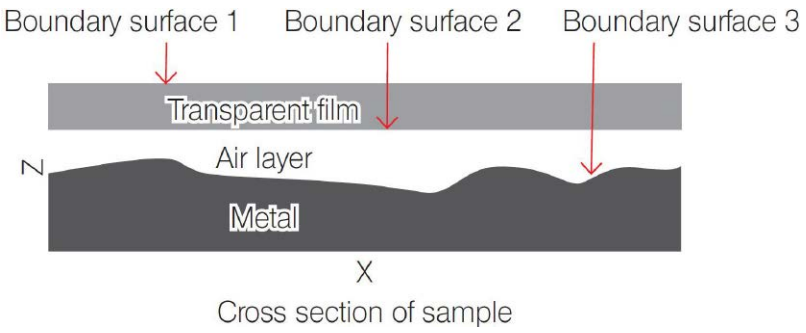

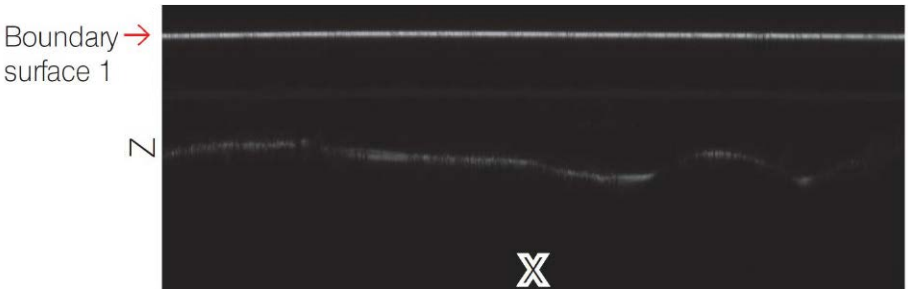

Reflected light intensity (when the filter is not used)

When the filter is not used

As the reflected light intensity on the top surface of the transparent film is strong, the boundary surface 1 is detected.

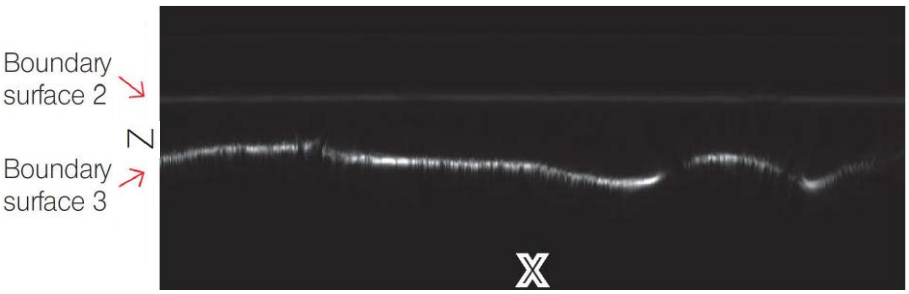

Reflected light intensity (when the filter is used)

When the filter is used

As the reflected light intensity on the top surface of the metal is strong, mainly the boundary surface 3 is detected.

TIP

Even though the filter is used, the boundary surface 2 may be detected from the area where the light reflected from the metal surface is weak in some cases.

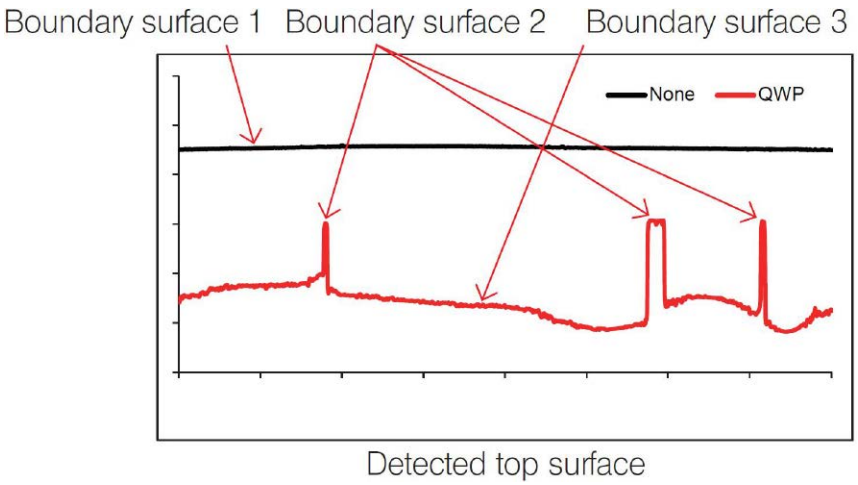

back to content

ADJUSTING THE SURFACE DETECTION FILTER

- Bring the sample top surface into focus approximately in advance and adjust the filter.
- The filter is adjusted for the first time only. It is not necessary to adjust the filter for the second time and after.

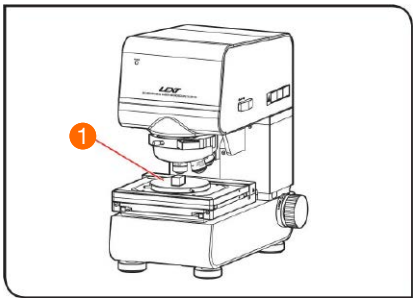

1 Place the mirror sample or the plain glass sample on the stage.

2 Engage the 10X objective in the light path.

3 Check the [Laser] checkbox in [1. Observe images] and start the laser observation.

◀ back to content

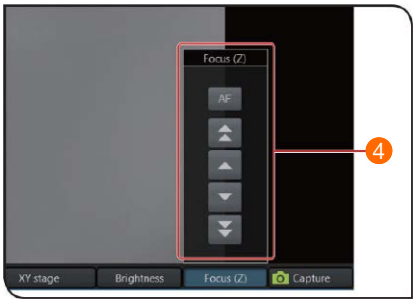

4 Bring the sample surface into focus.

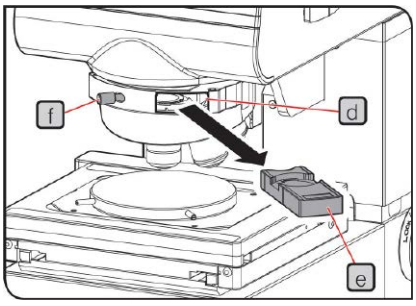

5 If the DIC slider U-DICR or the dummy slider [e] is attached to the slider insertion slot [d], loosen the mounting knob [f] to remove it.

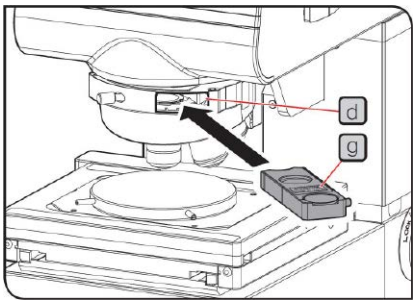

6 Insert the surface detection filter into the slider insertion slot [d] completely with the display surface [g] of the surface detection filter facing up.

TIP When the surface detection filter is engaged in the light path, the image becomes dark.

◀ back to content